Prediction of half-metallic gap formation and Fermi level position in Co-based Heusler alloy epitaxial thin films through anisotropic magnetoresistance effect

Varun K. Kushwaha,[1] S. Kokado,[2] S. Kasai,[1] Y. Miura,[1] T. Nakatani,[1] R. Kumara,[3] H. Tajiri,[3] T. Furubayashi,[1] K. Hono,[1] and Y. Sakuraba[1,*]

[1]National Institute for Materials Science, 1-2-1 Sengen, Tsukuba, Ibaraki 305-0047, Japan
[2]Graduate School of Integrated Science and Technology, Shizuoka University, Hamamatsu 432–8561, Japan
[3]Japan Synchrotron Radiation Research Institute, Sayo, Hyogo 679–5198, Japan

(Received 10 November 2021; revised 27 February 2022; accepted 31 May 2022; published 21 June 2022)

We have investigated the temperature (T) dependence of the anisotropic magnetoresistance (AMR) effect of $Co_2FeGa_{0.5}Ge_{0.5}$ (CFGG) epitaxial thin films having different compositions and atomic orders to examine the relation between AMR and the half-metallic electronic structure based on a developed theoretical model. The T dependence of the resistance change ($\Delta\rho$) of the AMR normalized at 10 K is minimal in the CFGG films having a standard composition and high atomic order. In contrast, the films having a large atomic disorder due to the Co-rich composition exhibit a large reduction of $\Delta\rho$ with T. Our theoretical model of AMR well explains this behavior; namely, the half-metallic ferromagnets having the Fermi level (E_F) around the center of the half-metallic gap are predicted to show a small T dependence of $\Delta\rho$ because of no/few localized $d\downarrow$ states at E_F. On the contrary, a large change of $\Delta\rho$ with T is expected for the half-metallic materials having E_F close to gap edges or large in-gap states because of the contribution of thermally excited s-d scattering involving the $d\downarrow$ states. Moreover, we have also investigated the variation of $\Delta\rho$ with T for the thin films of various half-metallic Co-based Heusler alloys and found the behavior that agrees with our theoretical prediction. The present study proves that the formation of a half-metallic gap and the position of E_F in a half-metallic material are readily predictable from the T dependence of $\Delta\rho$ of the AMR effect, which can be a facile way for efficient screening of half-metallic materials.

DOI: 10.1103/PhysRevMaterials.6.064411

I. INTRODUCTION

Half-metallic ferromagnets (HMFs) possess a band gap in one spin channel at the Fermi level (E_F) and thus exhibit 100% spin polarization (P) [1,2]. Achieving spin polarization close to 100% at room temperature (RT) could lead to a major innovation in spintronics; thus, HMFs have attracted strong research interest as potential key materials for various spintronics devices [3–5]. Among known classes of half-metallic materials, Co-based full Heusler alloys with a chemical formula of X_2YZ, where $X, Y =$ transition elements and $Z = p$-block elements, have attracted much attention due to their theoretically predicted half metallicity and high Curie temperature [6–8]. In the last decade, many studies have demonstrated the usefulness of the Co-based Heusler alloys in achieving giant magnetoresistance (GMR), large tunnel magnetoresistance, and large spin-accumulation signal in nonlocal spin-valve (NLSV) devices due to their half-metallic natures [9–22]. Despite the large MR ratio observed in the Co-based Heusler alloys, further enhancement of MR performance at RT is required for the usage in practical applications. According to theoretical studies, the electronic structure of half-metallic Heusler alloys is very sensitive to structural disorder [23–25]. The structural disorders give rise to the formation of some minority ($\downarrow$) states in the half-metallic gap, resulting in low spin polarization or a loss of half metallicity. However, usually it is not easy to investigate the effect of atomic disorder between X and Y neighboring elements as the atomic numbers of their constituent elements such as Cr, Mn, Fe, Co, and Ni are close to distinct using standard x-ray diffraction (XRD) techniques with Cu-K_α radiation source. In addition, the position of E_F in the half-metallic gap, i.e., near the center or the edges of the gap, is also a critical issue in half-metals that affects the temperature (T) dependence of P. However, there is no efficient experimental method to measure P and the position of E_F in half-metallic materials. In the past, the spin polarization of electric current (β) has been deduced from the transport properties of current-perpendicular-to-plane giant magnetoresistance (CPP-GMR) [15,16] and NLSV devices [14,26,27]. However, the device fabrication involving thin-film processing and microfabrication is very time-consuming. Another powerful technique is spin-resolved photoemission spectroscopy (SR-PES). Although large spin polarization over 93% was reported in the epitaxial Co_2MnSi thin film using SR-PES, careful sample preparation and analysis are required because of its strong surface sensitivity [28]. Hence, it is strongly desired to obtain information on spin polarization using a facile method. According to the extended two-current model of anisotropic magnetoresistance (AMR) effect with considering all s-d electron scattering processes through different spin channels,

*SAKURABA.Yuya@nims.go.jp

 ©2022 American Physical Society

which has been developed by Kokado *et al.* [29], the sign of AMR ratio should always be negative for a half-metal. Based on this theory, it was experimentally demonstrated that there is a close correlation between the AMR effect and spin polarization, thereby establishing it a facile way in search of new materials having high spin polarization [14,30–34]. However, in the previous studies, it was claimed that the negative AMR is only a necessary but not sufficient condition for half-metallic material; thus, it is not always straightforward to judge half-metallic nature only by the sign of AMR.

In this study, to deepen the understanding of a relationship between AMR and half-metallic electronic structure, we carefully analyzed the T dependence of the AMR effect of $Co_2FeGa_{0.5}Ge_{0.5}$ (CFGG) epitaxial thin film, which is known to have a half-metallic band gap based on the high spin polarization measured by the point-contact Andreev reflection technique [35], giant MR ratio in CPP-GMR [22], and large spin-accumulation signal in NLSV devices [13,26]. We measured T dependence of AMR for the CFGG films and analyzed the relationship of AMR with the half-metallic electronic structure based on the extended two-current model of AMR. In order to validate our arguments, we performed the synchrotron anomalous x-ray diffraction (AXRD) to analyze the atomic orders quantitatively and first-principles calculation of the density of states (DOS) based on the determined site occupation. We also fabricated the NLSV devices from the single-layer CFGG film that is the same for the AMR measurement to deduce β of the CFGG directly. Finally, the proposed method using AMR was extended to other Co-based Heusler films to confirm the validity of our analysis. The present result elucidated the formation of a half-metallic bandgap and the position of E_F is predictable from AMR measurements for the simple single-layer film without measurement of transport properties of the devices that require time-consuming microfabrication, which is beneficial for high-throughput screening of half-metallic materials.

II. EXPERIMENTAL AND CALCULATION DETAILS

In this study, we have prepared two series of CFGG films having different composition ratios using the CFGG alloy targets in an ultrahigh-vacuum magnetron sputtering system. Before thin-film deposition, the MgO substrate was cleaned by chemical washing (acetone→ethanol) followed by *in situ* Ar-ion milling to remove the surface contamination. All CFGG films were deposited at RT and subsequently annealed *in situ* at temperatures $T_{\mathrm{ann}} = 300 - 700\,^{\circ}\mathrm{C}$ for 30 min to induce atomic ordering. Two sets of films with 30 and 50 nm thickness were deposited for each composition. The chemical compositions of the films were analyzed by the inductive coupled plasma mass spectroscopy method. By tuning the deposition conditions, we obtained two series of films having largely different film compositions of 49:23:14:14 (at. %) and 54:26:11:9 (at. %), which indicates that the former is close to the previously reported CFGG composition [31,36], whereas the latter is richer in Co and poorer in Ge; hence, we referred them to as standard CFGG and Co-rich CFGG films, respectively. The crystal structure of the CFGG films and the disorder between Co and Fe atoms were studied by XRD with the ordinary Cu-K_α and synchrotron-radiated x-rays.

We microfabricated 30-nm-thick standard CFGG films into NLSV devices using electron-beam lithography, Ar-ion milling, and the lift-off techniques, and then β of CFGG films was estimated at RT by measuring the spin-accumulation signal (ΔR_S) in the copper (Cu) channel. Total 24 devices were prepared on the same substrate with different center-to-center distances (d) between two CFGG wires from 450 to 1350 nm. In order to control the relative magnetization configuration (parallel/antiparallel) of the CFGG wires by sweeping the magnetic field, these CFGG wires were patterned into different geometric aspect ratios. Then, these CFGG wires were isolated by sputtering a 30-nm-thick SiO_2 onto the milled area, followed by lifting off the remaining resist mask. In the next fabrication step, two CFGG wires were connected by a 100-nm-thick Cu channel deposited by an electron-beam (EB) evaporator. Prior to the deposition of the Cu channel, a soft *in situ* Ar-ion milling was performed to obtain a transparent contact at the CFGG/Cu interface. The resistance (R_i)-contact area (A_j) product, R_iA_j was found to be much less than $1\,\mathrm{m}\Omega\,\mu\mathrm{m}^2$ for all annealing temperatures, indicating a transparent contact [37] at the CFGG/Cu interface. Note that after cleaning of the surface of CFGG wires, the sample was transferred to the EB evaporator chamber without breaking the vacuum.

In order to investigate the sign and the magnitude of the AMR ratio, the 50-nm-thick CFGG films were patterned into Hall-bar geometry using photolithography and Ar-ion milling techniques. A motorized sample rotator attached with a Physical Property Measurement System was used for the AMR measurements. For evaluating AMR ratio, DC current (I_C) of 1 mA was applied to the $\langle 110 \rangle$ direction of the CFGG film, and the constant external magnetic field H of 300 mT was rotated within the film plane. The DC resistance change as a function of the relative angle between H and I_C (defined as ϕ) was measured at different T from 10 to 300 K. AMR ratio was evaluated by $\Delta\rho/\rho_\perp \times 100\%$, where $\Delta\rho = \rho_\parallel - \rho_\perp$, and $\rho_\parallel$ ($\rho_\perp$) is the resistivity of the film for $\phi = 0^\circ$ (90°).

Additionally, the spin-resolved DOS for the standard CFGG with different atomic orders were calculated at 0 K by first-principles calculations based on the density-functional theory using the Korringa-Kohn-Rostoker (KKR) method [38,39] implemented into the HUTSEPOT code [40]. The atomic disorder is treated within the coherent potential approximation (CPA), and the Kohn-Sham potential is determined by atomic-sphere approximation. For the exchange-correlation energy, we adopted a local spin-density approximation of Perdew-Wang [41] with the self-interaction correction [40] for the majority-spin Fe-t_{2g} orbital. Other technical details on the first-principles calculations are described in Ref. [34].

III. RESULTS AND DISCUSSION IN STANDARD CFGG FILMS

A. Structural analysis

XRD with Cu-K_α radiation ($\lambda = 1.5406\,\mathrm{\AA}$) was used to investigate the crystal structure, i.e., $B2$ and $L2_1$ order of the CFGG films. Figure 1(a) shows ω-2θ (out-of-plane) XRD profiles of the standard CFGG films annealed at $T_{\mathrm{ann}} = 300$–$700\,^{\circ}\mathrm{C}$. All films show clear 002 and 004 diffraction

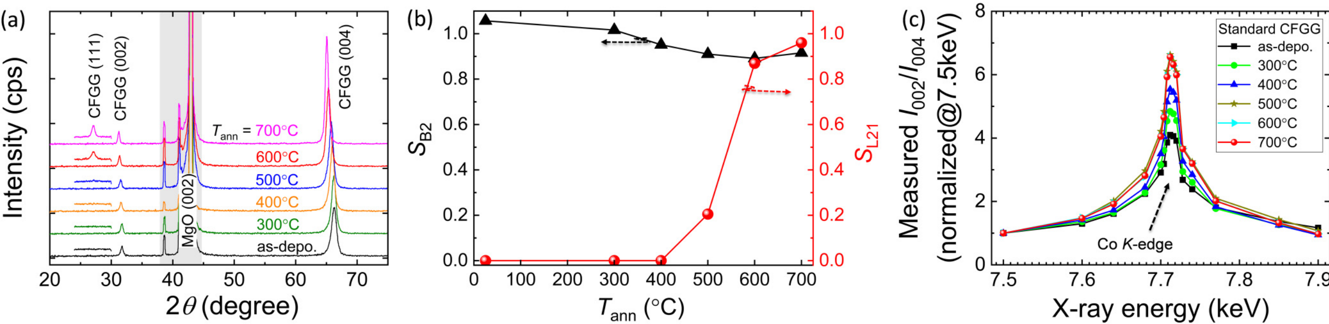

FIG. 1. (a) ω-2θ (out-of-plane, at $\chi = 0^\circ$) XRD patterns of CFGG thin films annealed at $T_{ann} = 300$–$700\ ^\circ$C. Additionally, ω-2θ-scan of 111 odd superlattice peak at tilt angle $\chi \approx 54.7^\circ$, which is appearing over 500 °C. The peaks highlighted by the light-gray color are appearing from the 002 diffraction from MgO substrate. (b) T_{ann} dependence of the degree of $B2$ ordering (S_{B2}) and $L2_1$ ordering (S_{L21}). (c) Experimentally measured x-ray energy dependence of I_{002}/I_{004} near Co-K edge for the standard CFGG films.

peaks other than the peaks from the MgO substrate, indicating the epitaxial film growth along the ⟨001⟩ direction. Clear 002 superlattice peak for all the films suggests the formation of a highly $B2$-ordered structure. In order to detect the 111 superlattice peak, which reflects the $L2_1$ order, films were tilted by 54.7° from the film-surface normal direction. The 111 superlattice peak is detected for $T_{ann} \geqslant 500\ ^\circ$C [Fig. 1(a)].

Next, we have estimated the degree of $B2$ (S_{B2}) and $L2_1$ ordering (S_{L21}) using the following expressions:

$$S_{B2} = \sqrt{\frac{I_{002}^{exp}/I_{004}^{exp}}{I_{002}^{sim}/I_{004}^{sim}}}, \quad (1)$$

and

$$S_{L2_1} = \sqrt{\frac{I_{111}^{exp}/I_{004}^{exp}}{I_{111}^{sim}/I_{004}^{sim}}}, \quad (2)$$

where I_{002}, I_{004}, and I_{111} represent the integrated intensities of 002, 004, and 111 diffraction peaks, respectively. Here, the superscript "exp (sim)" indicates the experimental (simulated) integrated x-ray intensity for a perfectly $L2_1$-ordered structure. The theoretical XRD intensity was simulated for actual CFGG film composition using the Visualization for Electronic and Structural Analysis (VESTA) software [42], considering a perfectly $L2_1$-ordered structure. It should be noted that the dispersive corrections were also taken into account during the XRD simulation. The estimated values of S_{B2} and S_{L21} as a function of T_{ann} are shown in Fig. 1(b), where the value of S_{B2} for the as-deposited film is slightly higher than 1 and decreases with increasing T_{ann}. On the other hand, S_{L21} is 0 for the as-deposited state and the annealed films at 300 and 400 °C and improved by annealing above 500 °C. The estimated values of S_{B2} and S_{L21} at 700 °C were found to be 0.92 and 0.96, respectively, indicating a high degree of $B2$ and $L2_1$ order. The value of S_{B2} for the as-deposited state is slightly higher than unity, implying the existence of disorder between Co and Fe atoms. However, the Co-Fe disordering level cannot be quantitatively estimated using an ordinary Cu-K_α radiation-based XRD system due to their very similar atomic scattering factors of Co and Fe atoms at the Cu-K_α energy. Thus, we performed AXRD experiments using a synchrotron radiation source at beamline BL13XU in SPring-8 [43,44]. Figure 1(c) displays the experimentally measured I_{002}/I_{004} ratio (normalized by the value at x-ray energy, $E = 7.5$ keV) of all CFGG films. One can clearly see that the peak at the Co-K edge increases with increasing T_{ann} and saturates above 500 °C. This result of AXRD measurement at Co-K edge is very similar to the previous report by Goto *et al.* [34] in CFGG films, indicating that the degree of Co-Fe order improves with increasing annealing temperature; high Co-Fe order is realized above 500 °C.

B. Electronic structure calculations

First-principles calculations were performed to investigate the effect of atomic disorder on the electronic structure of CFGG Heusler alloy. The atomic configurations for the theoretical calculations are tabulated in Table S1 in the Supplemental Material [45]. Figure 2(a) shows theoretically calculated spin-resolved DOS of a standard CFGG with different atomic orders. We found that both ideal $L2_1$- and $B2$-ordered CFGG have a half-metallic electronic structure, a finite-energy band gap exists between the bottom of the conduction band (CB) and top of the valence band (VB) in the minority-spin DOS, and the position of E_F is predicted to be almost in the center of this half-metallic gap, which agrees with previous studies [34,46]. We can clearly see that a large 50% Co-Fe disorder, i.e., 50% of Fe atoms occupy X site, destroys this half-metallic gap, suggesting that our CFGG film in the as-deposited state should lose its half-metallic nature. We also calculated the case with a 4% Co-Ga disorder corresponding to the imperfect $L2_1$ order with $S_{L21} = 0.96$ for $T_{ann} = 700\ ^\circ$C. Although tiny in-gap states are predicted to form near E_F, the half-metallic gap structure is still preserved in this case. Because spin-dependent transport is governed by the sp-conduction electron having a small effective mass, here we also show the local DOS (LDOS) of sp-electron (orbital) in Fig. 2(b). A clear half-metallic gap exists in all the cases except for the one with a large 50% Co-Fe disorder. The theoretically calculated spin polarization of sp electron LDOS (P_{sp}) is summarized in Fig. 2(c). P_{sp} is predicted to be 42% in the CFGG with large Co-Fe disorder, but it is enhanced with promoting Co-Fe atomic order; large P_{sp} of 93.7, 92.8, and 83.9% are obtained for the ideal $L2_1$, $B2$, and $L2_1$ with small 4% Co-Ga disorder, respectively. It should be mentioned here that there are finite DOS in the half-metallic gap even

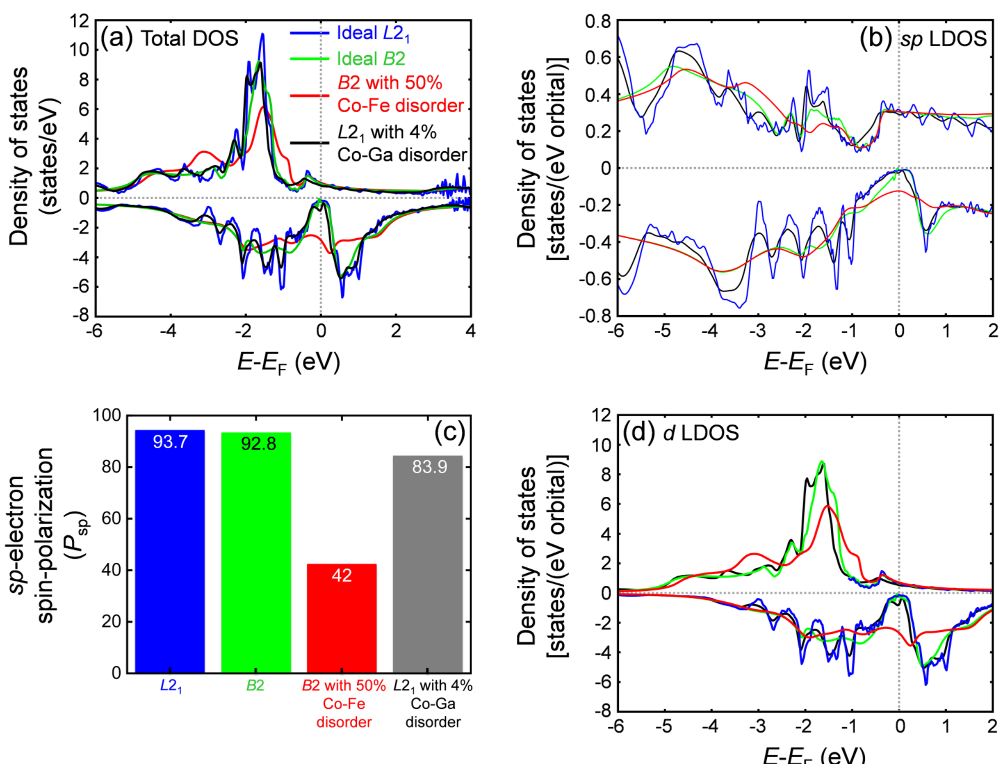

FIG. 2. Theoretically calculated majority and minority spin-resolved DOS of a standard CFGG for ideal $L2_1$ and $B2$ structures as well as for a $B2$ with Co-Fe (50%) and $L2_1$ with Co-Ga (4%) disorders. (a) Total DOS, (b) sp-electron LDOS, (c) spin polarization P_{sp} (%) of sp electrons, and (d) d-electron LDOS with different atomic orders.

in the $L2_1$-ordered CFGG. This is caused by the lifetime effect of eigenstates due to the spherical approximation for atomic potentials in KKR-CPA calculation, which generates a small uncertainty of theoretical P_{sp}. In addition, it is still controversial whether or not Coulomb interaction correction U should be incorporated in the first-principles calculation of DOS for half-metallic Heusler alloys. In the CFGG, it was reported that the half-metallic gap can be clearer with the lesser minority-spin state by adding U compared with the present result without U [46]. However, because the effect of Co-Fe and Co-Ga disorders on the half-metallic gap is expected to be qualitatively similar regardless of with and without U, the treatment of U does not affect the main argument on AMR in this study as an indicator to see a half-metallic gap and the formation of in-gap states.

C. Evaluation of spin-polarization in standard CFGG films

1. AMR

We measured the AMR effect at 10 and 300 K in 50-nm-thick CFGG epitaxial films annealed at different T_{ann}. Figure 3(a) shows the ϕ dependence of the AMR ratio measured at 300 K. All the samples show the negative sign of AMR ratio, and its magnitude increases with increasing T_{ann} at both 300 and 10 K, as summarized in Fig. 3(b). Here, we clearly see that the magnitude of negative AMR increases with T_{ann} [Fig. 3(b)], which shows a qualitative agreement with the spin-polarization β evaluated by the NLSV measurements shown later. Previously, Sakuraba *et al.* [31] also found a positive correlation between the magnitude of negative AMR and the MR output of the CPP-GMR devices. However, one can notice that negative AMR was observed even in the as-deposited film which should have a large in-gap state. Because the change in the AMR ratio $\Delta\rho/\rho$ is caused by the variation in resistivity ρ, here we focus on only resistance-change ($\Delta\rho$) of the AMR effect to perform a more straightforward analysis. $\Delta\rho$ vs T in the CFGG films for various T_{ann} is summarized in Fig. 3(c), where $\Delta\rho$ is normalized at 10 K. One can clearly see that the CFGG film in the as-deposited state shows the most significant reduction of $\Delta\rho$ with T, $\Delta\rho = 0.56$ at 300 K. This reduction gradually becomes smaller with increasing T_{ann} and finally $\Delta\rho$ becomes almost constant from 10 to 300 K in the CFGG films of $T_{\mathrm{ann}} > 500$ °C.

To understand the T dependence of $\Delta\rho$, we derive the expression of $\Delta\rho$ ($=\rho_\parallel - \rho_\perp$) using the two-current model for a system consisting of a spin-polarized s state and localized d states with spin-orbit interaction [29]. We here focus on half-metallic ferromagnets with the relation of $\rho_{\parallel,\uparrow} \ll \rho_{\parallel,\downarrow}$ and $\rho_{\perp,\uparrow} \ll \rho_{\perp,\downarrow}$, where $\rho_{\parallel,\sigma}$ ($\rho_{\perp,\sigma}$) represents a resistivity of the σ spin for $\phi = 0°$ (90°). Under the above relation, $\rho_\parallel$ and $\rho_\perp$ are approximately written by

$$\rho_\parallel = \frac{\rho_{\parallel,\uparrow}\rho_{\parallel,\downarrow}}{\rho_{\parallel,\uparrow}+\rho_{\parallel,\downarrow}} = \frac{\rho_{\parallel,\uparrow}\rho_{\parallel,\downarrow}}{\rho_{\parallel,\downarrow}\left(1+\frac{\rho_{\parallel,\uparrow}}{\rho_{\parallel,\downarrow}}\right)} \approx \rho_{\parallel,\uparrow}, \quad (3)$$

$$\rho_\perp = \frac{\rho_{\perp,\uparrow}\rho_{\perp,\downarrow}}{\rho_{\perp,\uparrow}+\rho_{\perp,\downarrow}} = \frac{\rho_{\perp,\uparrow}\rho_{\perp,\downarrow}}{\rho_{\perp,\downarrow}\left(1+\frac{\rho_{\perp,\uparrow}}{\rho_{\perp,\downarrow}}\right)} \approx \rho_{\perp,\uparrow}, \quad (4)$$

and then $\Delta\rho$ becomes

$$\Delta\rho \approx \rho_{\parallel,\uparrow} - \rho_{\perp,\uparrow}. \quad (5)$$

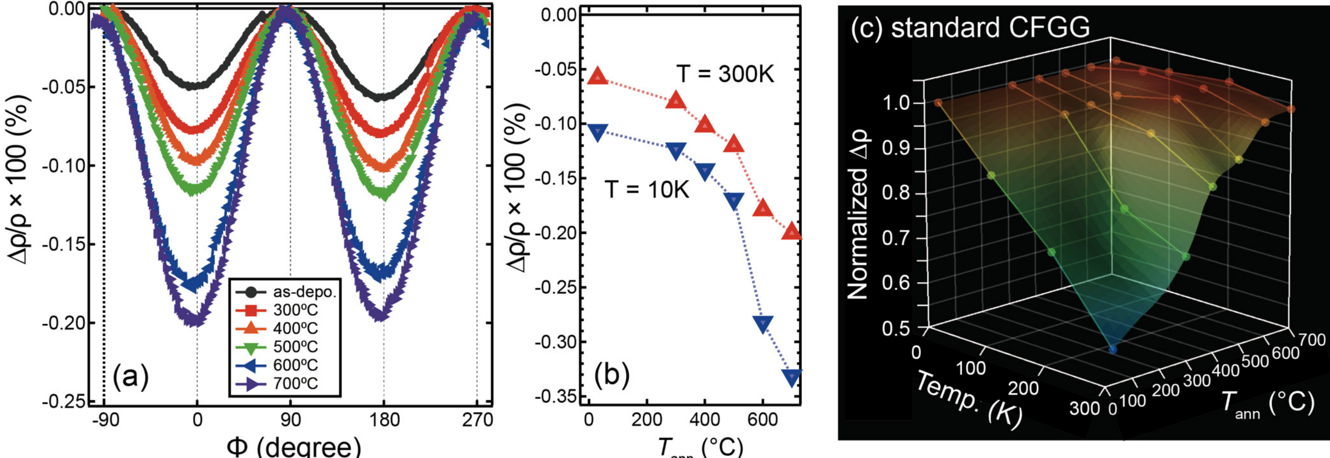

FIG. 3. (a) ϕ dependence of AMR ratio in epitaxial CFGG films measured at 300 K. (b) Summary of AMR ratio as a function of $T_{\rm ann}$. (c) T dependence of $\Delta\rho$ (normalized at 10 K) of AMR effect in standard CFGG films for various $T_{\rm ann}$.

By using Eqs. (22) and (24) in Ref. [29], $\Delta\rho$ is expressed as

$$\Delta\rho \approx \gamma(\rho_{s,\uparrow\to d,\downarrow} - \rho_{s,\uparrow\to d,\uparrow})$$
$$= -\gamma C D_{\uparrow}^{(d)}(E_{\rm F})\left(1 - \frac{D_{\downarrow}^{(d)}(E_{\rm F})}{D_{\uparrow}^{(d)}(E_{\rm F})}\right), \tag{6}$$

with

$$\rho_{s,\uparrow\to d,\varsigma} = \frac{m_{\uparrow}^{*}}{n_{\uparrow}e^{2}}\frac{2\pi}{\hbar}n_{\rm imp}N_{\rm n}|V_{s\uparrow\to d\uparrow}|^{2}D_{\varsigma}^{(d)}(E_{\rm F})$$
$$C = \frac{m_{\uparrow}^{*}}{n_{\uparrow}e^{2}}\frac{2\pi}{\hbar}n_{\rm imp}N_{\rm n}|V_{s\uparrow\to d\uparrow}|^{2}$$
$$\gamma = (3/4)(\lambda/H_{ex})^{2}, \tag{7}$$

where $\rho_{s,\uparrow\to d,\varsigma}$ is a resistivity for the s-d scattering from the s electron of $\uparrow$ spin to the localized d states of the ς spin. The quantity $n_{\rm imp}$ is the number density of impurities, $N_{\rm n}$ is the number of nearest-neighbor host atoms around the impurity, e is the electronic charge, and $\hbar$ is the Planck constant h divided by 2π. The quantities $m_{\uparrow}^{*}$ and $n_{\uparrow}$ are the effective mass and the number density of the electrons in the conduction band of the $\uparrow$ spin, respectively. The quantity $V_{s\uparrow\to d\uparrow}$ is the matrix element for the s-d scattering from $s\uparrow$ to $d\uparrow$ states due to the nonmagnetic impurities, and $D_{\varsigma}^{(d)}(E_{\rm F})$ is the DOS of the d state of ς spin around $E_{\rm F}$ that contributes to the s-d scattering. In addition, λ is the spin-orbit coupling constant, and $H_{\rm ex}$ is the exchange field of the ferromagnet. Here, γ and C are the parameters that are almost independent of the temperature. Thus, the T dependence of $D_{\varsigma}^{(d)}(E_{\rm F})$ is expected to affect the variation in $\Delta\rho$ with T predominantly because $D_{\varsigma}^{(d)}(E_{\rm F})$ can be considered as a parameter that changes with T due to the thermally excited electron occupation dependent on the Fermi distribution function [$f(E)$]. As can be seen in the theoretically calculated partial sp and d states [Figs. 2(b) and 2(d)], the $d\uparrow$ states are small and almost constant with respect to the energy around $E_{\rm F}$ in all cases with different atomic orders. The temperature T dependence of the $D_{\uparrow}^{(d)}(E_{\rm F})$ for CFGG using the disordered local moment method predicted a very small variation of the $\uparrow$-spin DOS with the temperature near $E_{\rm F}$ [47]. Therefore, it is reasonable to consider that the T dependence of $\Delta\rho$ mainly arises from that of $D_{\downarrow}^{(d)}(E_{\rm F})$ in the CFGG regardless of its atomic order. In the CFGG without Co-Fe disorder, because clear half-metallic gap forms and the position of the $E_{\rm F}$ is located around the center of the gap [see Fig. 2(a)], $D_{\downarrow}^{(d)}(E_{\rm F})$ must be almost zero and does not increase with T up to RT. Therefore, $\Delta\rho$ is expected to be almost constant with T in the CFGG films having the half-metallic gap. On the other hand, in the CFGG with Co-Fe disorder, largely localized $d\downarrow$ states appear in the half-metallic gap, as shown in Fig. 2(d). In this case, the expression of AMR in Eq. (6) is not applicable anymore, and various s-d scattering processes ($s\uparrow\to d\downarrow$, $s\downarrow\to d\downarrow$, and $s\downarrow\to d\uparrow$ as well as $s\uparrow\to d\uparrow$) determine the $\Delta\rho$, resulting in the remarkable T dependence of $\Delta\rho$ through the thermally activated changes in all processes. Therefore, on the basis of Eq. (6), we give a qualitative explanation for the overall trend of the observed T dependence of $\Delta\rho$ in the CFGG films. Namely, the $D_{\downarrow}^{(d)}(E_{\rm F})$ must be large in the CFGG film in as-deposited state [Fig. 2(d)] due to the Co-Fe disorder, which causes a large reduction of the $\Delta\rho$ with increasing T. Since the $D_{\downarrow}^{(d)}(E_{\rm F})$ gradually reduces with increasing $T_{\rm ann}$ by improved Co-Fe and $L2_1$-atomic ordering, and the half-metallic gap finally forms, $\Delta\rho$ becomes T independent at $T_{\rm ann} = 600$ and 700 °C.

This analysis of the T dependence of $\Delta\rho$ can be widely applied for various half-metallic Heusler alloys having a similar electronic structure. Not only the formation of a half-metallic gap but also the position of $E_{\rm F}$ can be deduced, which is understood by a possible s-d scattering process and its thermal excitation, as schematically explained in Fig. 4. In the case of the half-metallic material having the gap in $\downarrow$ states, $\Delta\rho$ is expressed as $\Delta\rho \approx \gamma(\rho_{s,\uparrow\to d,\downarrow} - \rho_{s,\uparrow\to d,\uparrow})$, from Eqs. (6) and (7). In the half-metallic Heusler alloy having a clear half-metallic gap and $E_{\rm F}$ around the center of the gap, only the $s\uparrow\to d\uparrow$ scattering process is allowed from zero to finite temperature around RT because of insufficient thermal excitation energy to generate $s\uparrow\to d\downarrow$ [Fig. 4(a)]. In this case, $\Delta\rho$ is expressed as $-\gamma\rho_{s,\uparrow\to d,\uparrow}$; thus, $\Delta\rho$ must be negative

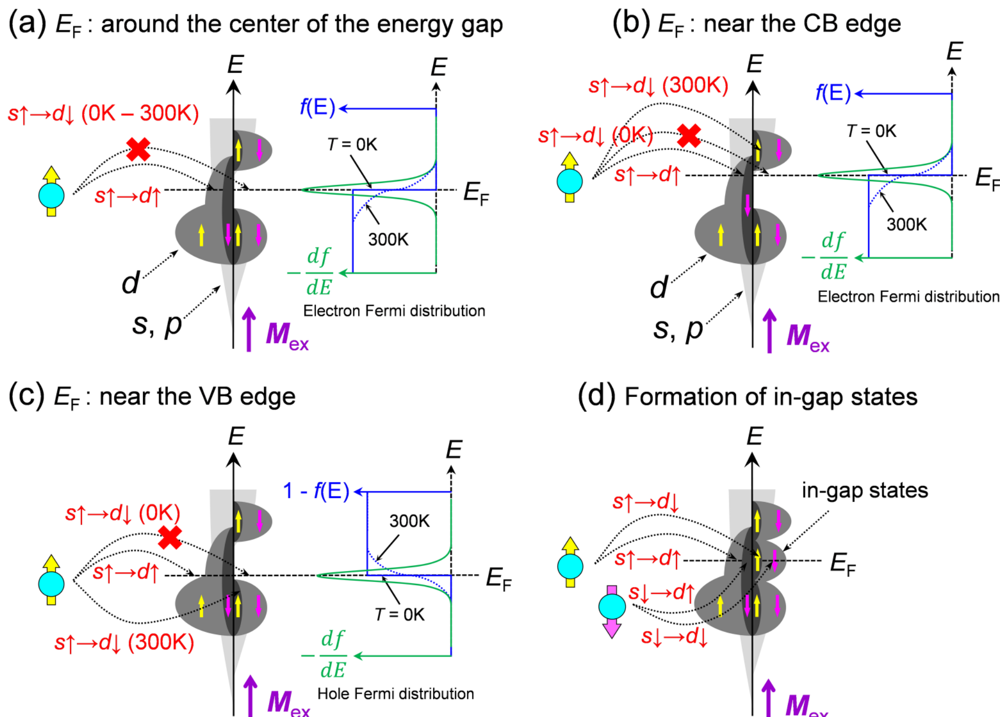

FIG. 4. Schematic illustration of partial spin-resolved DOS of s, p, and d states of a well-ordered Co-based Heusler alloy (half metallic) (a)–(c), and disordered one (d). The $sp\uparrow$ and $d\uparrow$ states are small and almost constant around E_F in all cases with different atomic orders; in contrast, a significant amount of $sp\downarrow$ and $d\downarrow$ states exist at E_F with Co-Fe disorder, as predicted theoretically. The dark-gray and light-gray areas denote the d-band and sp-band DOS, respectively, where sp-bands are partially covered by the d bands. The d band consists of both conductive and localized d states. In the scattering process, gray area of the DOS corresponds to the dominant components, while the black area of DOS to the slightly hybridized components. In the case of well-ordered CFGG, when E_F is around the center of the gap, only $s\uparrow\rightarrow d\uparrow$ scattering process is allowed from 0 to 300 K because of insufficient thermal excitation energy to generate $s\uparrow\rightarrow d\downarrow$ (a); and, when E_F exists around the vicinity of VB or CB edge, the $s\uparrow\rightarrow d\downarrow$ scattering process is also thermally activated at finite temperature (300 K) (b), (c). In contrast, in a disordered CFGG alloy, which exhibits both minority ($\downarrow$)-spin and majority ($\uparrow$)-spin states at E_F, not only $s\uparrow\rightarrow d\uparrow$ scattering but also other scattering processes ($s\uparrow\rightarrow d\downarrow$, $s\downarrow\rightarrow d\downarrow$, and $s\downarrow\rightarrow d\uparrow$) are significant (d). The direction of M_{ex} denotes the magnetization direction. $f(E)$ and $1-f(E)$ are the Fermi distribution functions which give the probability of an electron and a hole to occupy a state with energy (E), respectively. Solid and dashed blue lines denote the $f(E)$ at 0 K and higher temperature (>300 K), respectively. The solid green line represents the derivative of $-f(E)$ with respect to E, i.e., $-\frac{df(E)}{dE}$ at 300 K.

and shows very small T dependence as we observed in the standard CFGG film annealed at 600 and 700 °C. In the case of half-metallic Heusler alloys having the E_F around the vicinity of the VB or CB edge of the half-metallic gap, the $s\uparrow\rightarrow d\downarrow$ scattering process is thermally activated at finite temperature; thus, the magnitude of $\Delta\rho$ gradually decreases with T by the contribution of $\rho_{s,\uparrow\rightarrow d,\downarrow}$ [Figs. 4(b) and 4(c)]. When the in-gap states largely form because of atomic disorder, various s-d scatterings contribute to the $\Delta\rho$; thus, $\Delta\rho$ largely changes with T as observed in the standard CFGG in the as-deposited state.

2. Spin-accumulation signal (ΔR_S)

To investigate validity of the above-mentioned analysis of the $\Delta\rho$ of the AMR, we measured ΔR_S in the Cu channel using microfabricated NLSV devices and evaluate the spin polarization of electric current β. A schematic diagram of an NLSV measurement is shown in Fig. 5(a), where a nonmagnetic wire (N) orthogonally connects two ferromagnetic (FM) wires. NLSV devices were prepared by microfabricating the single-layer 30-nm-thick standard CFGG films. This NLSV device consists of two laterally separated CFGG wires (called spin injector and spin detector) bridged by a Cu channel, as shown in Fig. 5(b). Figure 5(c) shows electrical resistivities of CFGG (ρ_{CFGG}), and Cu (ρ_{Cu}) wires measured at RT as a function of annealing temperature T_{ann}. The ρ_{CFGG} decreases with increasing T_{ann} due to the improvement in the degree of $L2_1$ order in the CFGG films. The ρ_{Cu} of the Cu wire is almost constant in all devices within the range of 3 to 4 $\mu\Omega$ cm and the averaged ρ_{Cu} was found to be around 3.87 $\mu\Omega$ cm, which is very close to the previously reported value [26]. The nonlocal measurements were performed at RT by a conventional DC method with a current I_C of 0.5 mA, as displayed in Fig. 5(b), where the external magnetic field H was applied parallel to the long axis of the CFGG wires. I_C flows from one CFGG wire to the left-side Cu wire; as a result, (left-side) CFGG wire drives a spin-polarized current (I_S) into the Cu strips at the interface. This spin-polarized current diffuses through the Cu channel and accumulates at the second (right-side) CFGG/Cu interface that works as a detector. The accumulated spins at the second CFGG/Cu interface are detected by

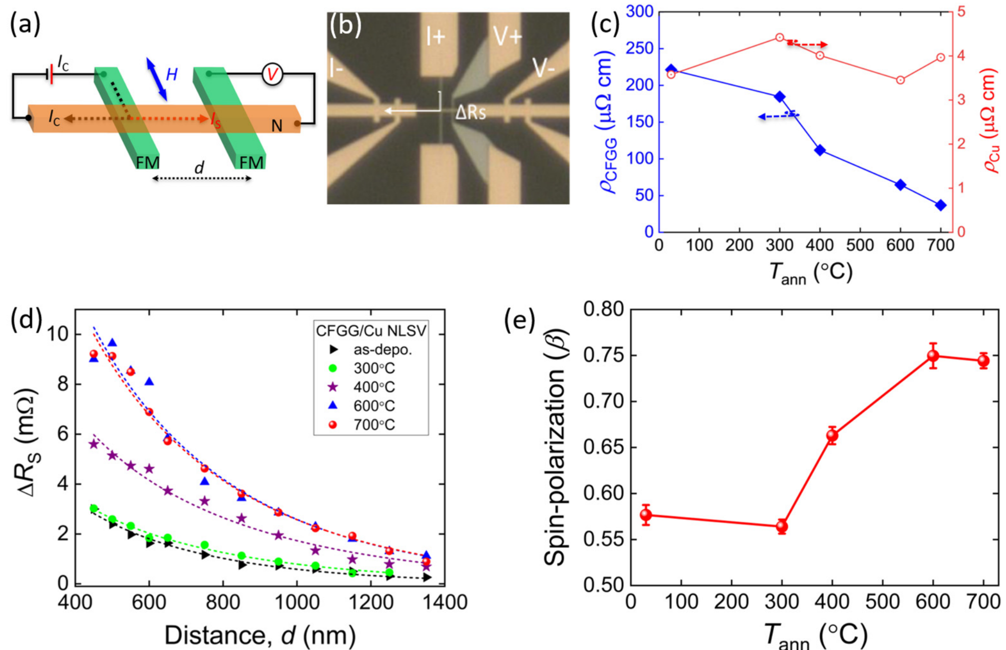

FIG. 5. (a) Schematic diagram of an NLSV device and the electrical scheme for nonlocal measurement. (b) Optical image of a fabricated CFGG/Cu NLSV device. (c) Estimated ρ_{CFGG} and ρ_{Cu} values as a function of T_{ann}. (d) Center-to-center distance d dependence of ΔR_S signal measured at 300 K in CFGG/Cu-based NLSV devices. The dashed line denotes the fitted ΔR_S-d result by Eq. (8). (e) The evaluated β at 300 K of CFGG films against T_{ann}. The error bar corresponds to the standard deviation of β.

measuring the output voltage (V) between the second CFGG and Cu wires. The measured signal $\Delta R_S = \Delta V/I_C$ decreases exponentially with increasing d because of the spin relaxation [Fig. 5(d)], where ΔV is the output voltage difference between parallel and antiparallel configuration of CFGG wires. The d dependence of measured ΔR_S increases with increasing T_{ann}, indicating the enhancement of spin polarization P due to the improved Co-Fe atomic ordering. In order to evaluate the β value, the measured ΔR_S-d result was fitted by the one-dimensional spin-diffusion model [37] for a transparent interface, expressed as

$$\Delta R_S = 4R_{Cu}\frac{\left(\frac{\beta}{1-\beta^2}\ \frac{R_{CFGG}}{R_{Cu}}\right)^2 e^{\left(-\frac{d}{\lambda_{Cu}}\right)}}{\left(1+\frac{2}{1-\beta^2}\ \frac{R_{CFGG}}{R_{Cu}}\right)^2 - e^{\left(-\frac{2d}{\lambda_{Cu}}\right)}}, \qquad (8)$$

where R_{CFGG} $(=\rho_{CFGG}\lambda_{CFGG}/A_J)$ and $R_{Cu}(=\rho_{Cu}\lambda_{Cu}/A_{Cu})$ are the spin resistance of CFGG and Cu, respectively. $\rho_{CFGG(Cu)}$, $\lambda_{CFGG(Cu)}$, A_J, and A_{Cu} represent the resistivity of CFGG (Cu), the spin-diffusion length of CFGG (Cu), the area of CFGG/Cu interface, and the cross-sectional area of the Cu wire, respectively. From the scanning electron microscopy image, the width of CFGG wires and the Cu channel is about 150 and 167 nm, respectively. For fitting the ΔR_S-d data, we used the value of λ_{CFGG} by assuming the $\rho_{CFGG}\lambda_{CFGG}$ is the same as the value reported for the $Co_2FeAl_{0.5}Si_{0.5}$ (CFAS), $\rho_{CFAS}\lambda_{CFAS} = 1.56\,\text{m}\Omega\,\mu\text{m}^2$, because CFAS is also predicted to be a half-metal having the same valence electron number (N_V) as CFGG [16] and λ has the inverse proportional relationship with the ρ [48]. Because the quality of the Cu channel should be the same in all devices, we used the same λ_{Cu} for all the devices. The β was evaluated by fitting the ΔR_S-d curves with an average λ_{Cu} value of 424 nm. This λ_{Cu} value is in good agreement with the previous report [13]. The β of CFGG is enlarged from 0.57 ± 0.01 for an as-deposited state to 0.74 ± 0.01 for the sample annealed at 700 °C due to the improvement in Co-Fe atomic order as summarized in Fig. 5(e). These results show a clear correlation between Co-Fe atomic order and the spin polarization evaluated by the NLSV devices. Furthermore, this enlargement in β from 57% (as deposited) to 74% (700 °C) agrees with the theoretically calculated P_{sp} of 42% and 83.9% for a $B2$ structure with 50% Co-Fe and $L2_1$ with 4% Co-Ga disorders, respectively [see Fig. 2(c)]. This result qualitatively agrees with the analysis performed on the $\Delta\rho$ vs T; β increases with T_{ann} and shows almost the same values at 600 and 700 °C.

IV. RESULTS AND DISCUSSION OF Co-RICH CFGG FILMS

In order to confirm the relationship between the T dependence of $\Delta\rho$ and the half-metallic electronic structure, we have also analyzed the atomic order and measured the T dependence of $\Delta\rho$ in the Co-rich CFGG film (50 nm). We first performed XRD (see Supplemental Material [45]) and AXRD (Fig. 6) measurements of the Co-rich film to know the crystal structure and the qualitative amount of Co antisite. The XRD results confirm that the Co-rich CFGG films also have similar (001)-oriented epitaxial growth and exhibit $L2_1$ ordering above 500 °C. Prior to the AXRD measurements, we simulated the integrated intensity (I_{111}) of 111 peaks [33] of a standard CFGG sample with various Co-Fe disorder levels $(x) = 0$–0.50 as a function of x-ray energy ranging from 7.5 to 7.9 keV at Co-K absorption edge [Fig. 6(a)]. We found that the I_{111} amplitude gradually increases with increasing x due to Co antisite. As standard and Co-rich CFGG films do not show 111 peaks below 500 °C, the AXRD measurements were carried

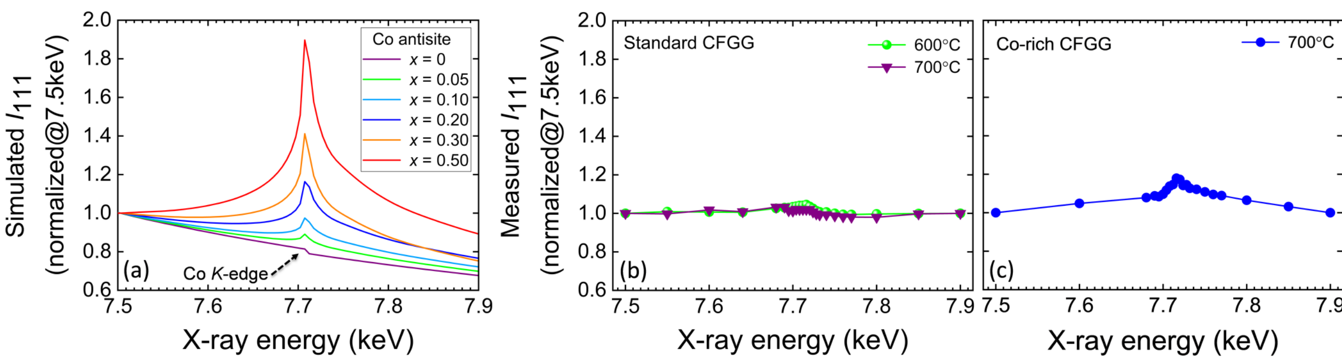

FIG. 6. (a) Simulated x-ray energy dependence of I_{111} at Co-K absorption edge of a standard CFGG sample with Co-Fe disorder level x. (b) Experimentally measured x-ray energy dependence of I_{111} at Co-K edge for standard CFGG ($T_{\mathrm{ann}} = 600$ and 700 °C), and (c) Co-rich CFGG film (700 °C).

out for 600 and 700 °C annealed films at around the Co-K edge [Figs. 6(b) and 6(c)]. The standard CFGG film's peak intensity at the Co-K edge energy is minimal. In contrast, the Co-rich one exhibits a relatively large intensity, indicating a larger amount of Co atoms in the Y site even after annealing at 700 °C compared with the former standard CFGG films. Because the excess 4% of the Co atoms must occupy the Y site becoming Co antisites, almost 10–20% of the Y site should be occupied by Co atoms, which is consistent with the experimental result.

Figure 7 shows the T dependence of $\Delta\rho$ of the AMR effect normalized at 10 K in the Co-rich CFGG films. All the films show the negative AMR ratio in the whole range of T_{ann}, similar to the standard CFGG films; large T dependence of $\Delta\rho$ is observed in all the films even with $T_{\mathrm{ann}} = 600$ and 700 °C. Because of the unavoidable formation of the Co antisites in the Co-rich CFGG as confirmed by AXRD, the localized $d\downarrow$ states inevitably form in the half-metallic gap [corresponds to the case shown in Fig. 4(d)] in these Co-rich CFGG films regardless of the T_{ann}. Therefore, this large T dependence of $\Delta\rho$ supports our argument. Namely, the T dependence of $\Delta\rho$ of the AMR effect is sensitive to the formation/disappearance of the half-metallic gap in CFGG, which can be applied to any other half-metallic materials having a similar electronic structure. Here, someone might be concerned about the extrinsic effect such as the defects, grain boundaries, and the surface on the observed annealing temperature dependence of AMR effect in present CFGG films because previously many studies reported that the annealing process induces large variation in AMR in various polycrystalline and granular ferromagnetic films, especially when the thickness of the film is less than a few tens of nanometers [49–52]. However, because the present standard and Co-rich CFGG films are sufficiently thick (50 nm) and have a homogeneous epitaxial structure even in the as-deposited state, such extrinsic effect on the AMR is expected to be much smaller than the intrinsic electronic structure. Our previous studies on the AMR in Heusler epitaxial films [14,33] and the results shown in the next section also support a strong relationship between observed AMR and intrinsic electronic structure.

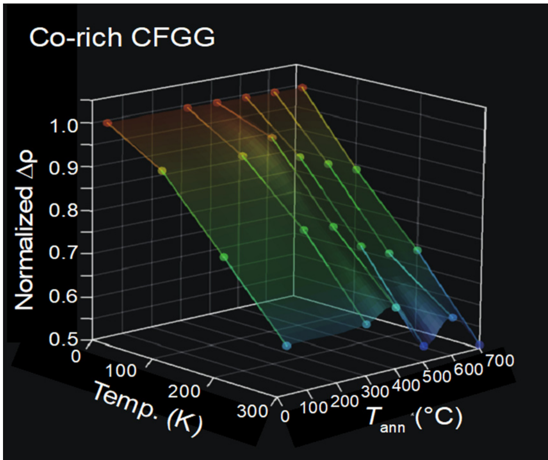

FIG. 7. T dependence of $\Delta\rho$ (normalized at 10 K) values for Co-rich CFGG films for various T_{ann}.

V. RESULTS AND DISCUSSION IN VARIOUS Co-BASED HEUSLER ALLOYS

In earlier study, we have investigated the AMR effect of the (001)-oriented epitaxial thin films of various Co-based Heusler alloys [$Co_2MnAl_{1-x}Si_x$ (CMAS), $Co_2MnGa_{0.25}Ge_{0.75}$ (CMGG), $Co_2FeGa_{0.25}Si_{0.75}$ (CFGaS), $Co_2FeGe_{0.25}Si_{0.75}$ (CFGeS), and Co_2FeSi (CFS)] [31]. Here, we analyzed the T dependence of $\Delta\rho$ in these films and summarized it as a function of their N_{V} (see Fig. 8). As we reported earlier [31], the sign of AMR changes with N_{V} from positive to negative at around 28.2 and then becomes positive again around 30.3, suggesting E_{F} moves from the VB edge to the CB edge with increasing N_{V}. Interestingly, the T dependence of $\Delta\rho$ agrees well with the prediction shown in Figs. 4(a)–4(c). Namely, the Co-based Heusler alloy films that are expected to have E_{F} around the center of half-metallic gaps such as CMS, CFGG, and CMGG show almost constant $\Delta\rho$ regardless of T, whereas the films having E_{F} close to the gap edges, such as CMAS with $x = 0.2$ and CFGeS, clearly show a large reduction of $\Delta\rho$ with temperature. We found an enlargement of $\Delta\rho$ with increasing the T in only CMA, which could be attributed to the complex s-d scattering process in this material due to large $d\uparrow$ and $s\downarrow$ states at the E_{F}.

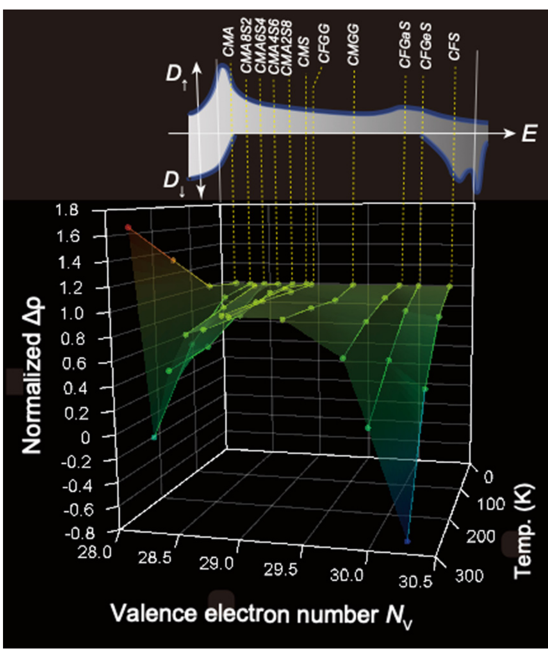

FIG. 8. Valence electron number N_{V} dependence of $\Delta\rho$ (normalized at 10 K) values for various Co-based Heusler alloys.

VI. CONCLUSIONS

In conclusion, we measured the T dependence of the AMR effect in CFGG and various Co-based Heusler films to investigate its relationship with the half-metallic electronic structure. It was found that the magnitude of the negative AMR ratio in the standard CFGG film shows a similar annealing temperature dependence with the spin polarization of β evaluated from the nonlocal spin valve. In addition, CFGG film with high Co-Fe order shows a small T dependence of $\Delta\rho$, but the one with a high disorder or Co antisites always exhibits large T dependence. The developed theoretical model explains such tendency in the T dependence of $\Delta\rho$. Namely, the half-metallic materials having the E_{F} around the center of the half-metallic gap are predicted to show a small T dependence of $\Delta\rho$ because of no/few localized $d\downarrow$ states at E_{F}; in contrast, a large change of $\Delta\rho$ is expected for those half-metallic materials having E_{F} close to gap edges or large in-gap states because of the contribution of thermally excited *s-d* scattering involving the $d\downarrow$ states. We also found that this theoretical prediction agrees well with the T dependence of $\Delta\rho$ of other Co-based half-metallic Heusler thin films. The present study elucidates that the T dependence of $\Delta\rho$ of the AMR effect gives us a view of not only the formation of a half-metallic gap but also the position of E_{F} without time-consuming transport measurements of any microfabricated devices. Therefore, the measurement of the T dependence of $\Delta\rho$ of the AMR effect is useful for the high-throughput screening of half-metallic Heusler alloys.

ACKNOWLEDGMENTS

The authors thank B. Masaoka and N. Kojima for technical support for the microfabrication process and the measurement of NLSV devices. This work was supported by a Grant-in-Aid for Scientific Research (S) (Grant No. 17H06152) and (B) (Grant No. 21H01608) from the Japan Society for the Promotion of Science (JSPS) and JST, CREST (Grant No. JPMJCR21O1). The AXRD measurements were performed on the beamline BL13XU at SPring-8 with the approval of the Japan Synchrotron Radiation Research Institute (JASRI) under Proposals No. 2018A1231, No. 2018B1162, and No. 2019B1138.

[1] R. A. de Groot, F. M. Mueller, P. G. van Engen, and K. H. J. Buschow, Phys. Rev. Lett. **50**, 2024 (1983).
[2] An ideal "half-metal" or "half-metallic ferromagnet" has a finite majority spin-up and zero minority spin-down density of states at the Fermi level or vice versa, resulting in 100% spin polarization. However, almost all previous studies have claimed half-metallic material if the measured spin polarization is sufficiently large. Therefore, in this paper, we have also called the material showing a large spin polarization originating from the half-metallic energy gap as half-metal or half-metallic, even though complete 100% spin polarization is not obtained.
[3] I. Žutic, J. Fabian, and S. Das Sarma, Rev. Mod. Phys. **76**, 323 (2004).
[4] S. A. Wolf, D. D. Awschalom, R. A. Buhrman, J. M. Daughton, S. von Molnár, M. L. Roukes, A. Y. Chtchelkanova, and D. M. Treger, Science **294**, 1488 (2001).
[5] A. Hirohata and K. Takanashi, J. Phys. D: Appl. Phys. **47**, 193001 (2014).
[6] I. Galanakis, P. H. Dederichs, and N. Papanikolaou, Phys. Rev. B **66**, 174429 (2002).
[7] B. Balke, S. Ouardi, T. Graf, J. Barth, C. G. F. Blum, G. H. Fecher, A. Shkabko, A. Weidenkaff, and C. Felser, Solid State Commun. **150**, 529 (2010).
[8] S. Wurmehl, G. H. Fecher, H. C. Kandpal, V. Ksenofontov, C. Felser, H.-J. Lin, and J. Morais, Phys. Rev. B **72**, 184434 (2005).
[9] S. Kämmerer, A. Thomas, A. Hütten, and G. Reiss, Appl. Phys. Lett. **85**, 79 (2004).
[10] Y. Sakuraba, M. Hattori, M. Oogane, Y. Ando, H. Kato, A. Sakuma, T. Miyazaki, and H. Kubota, Appl. Phys. Lett. **88**, 192508 (2006).
[11] M. J. Carey, S. Maat, S. Chandrashekariaih, J. A. Katine, W. Chen, B. York, and J. R. Childress, J. Appl. Phys. **109**, 093912 (2011).
[12] Ikhtiar, S. Kasai, A. Itoh, Y. K. Takahashi, T. Ohkubo, S. Mitani, and K. Hono, J. Appl. Phys. **115**, 173912 (2014).
[13] Y. K. Takahashi, S. Kasai, S. Hirayama, S. Mitani, and K. Hono, Appl. Phys. Lett. **100**, 052405 (2012).
[14] J. Chen, Y. Sakuraba, K. Masuda, Y. Miura, S. Li, S. Kasai, T. Furubayashi, and K. Hono, Appl. Phys. Lett. **110**, 242401 (2017).
[15] Y. Sakuraba, K. Izumi, T. Iwase, S. Bosu, K. Saito, K. Takanashi, Y. Miura, K. Futatsukawa, K. Abe, and M. Shirai, Phys. Rev. B **82**, 094444 (2010).

[16] T. M. Nakatani, T. Furubayashi, S. Kasai, H. Sukegawa, Y. K. Takahashi, S. Mitani, and K. Hono, Appl. Phys. Lett. **96**, 212501 (2010).
[17] J. Sato, M. Oogane, H. Naganuma, and Y. Ando, Appl. Phys. Express **4**, 113005 (2011).
[18] Z. Diao, M. Chapline, Y. Zheng, C. Kaiser, A. Ghosh Roy, C. J. Chien, C. Shang, Y. Ding, C. Yang, D. Mauri, Q. Leng, M. Pakala, M. Oogane, and Y. Ando, J. Magn. Magn. Mater. **356**, 73 (2014).
[19] H. Liu, Y. Honda, T. Taira, K. Matsuda, M. Arita, T. Uemura, and M. Yamamoto, Appl. Phys. Lett. **101**, 132418 (2012).
[20] Y. Sakuraba, M. Ueda, Y. Miura, K. Sato, S. Bosu, K. Saito, M. Shirai, T. J. Konno, and K. Takanashi, Appl. Phys. Lett. **101**, 252408 (2012).
[21] Y. K. Takahashi, N. Hase, M. Kodzuka, A. Itoh, T. Koganezawa, T. Furubayashi, S. Li, B. S. D. C. S. Varaprasad, T. Ohkubo, and K. Hono, J. Appl. Phys. **113**, 223901 (2013).
[22] S. Li, Y. K. Takahashi, T. Furubayashi, and K. Hono, Appl. Phys. Lett. **103**, 042405 (2013).
[23] S. Picozzi, A. Continenza, and A. J. Freeman, Phys. Rev. B **69**, 094423 (2004).
[24] M. P. Raphael, B. Ravel, Q. Huang, M. A. Willard, S. F. Cheng, B. N. Das, R. M. Stroud, K. M. Bussmann, J. H. Claassen, and V. G. Harris, Phys. Rev. B **66**, 104429 (2002).
[25] Y. Miura, K. Nagao, and M. Shirai, Phys. Rev. B **69**, 144413 (2004).
[26] Ikhtiar, S. Kasai, Y. K. Takahashi, T. Furubayashi, S. Mitani, and K. Hono, Appl. Phys. Lett. **108**, 062401 (2016).
[27] K. Hamaya, N. Hashimoto, S. Oki, S. Yamada, M. Miyao, and T. Kimura, Phys. Rev. B **85**, 100404(R) (2012).
[28] M. Jourdan, J. Minár, J. Braun, A. Kronenberg, S. Chadov, B. Balke, A. Gloskovskii, M. Kolbe, H. J. Elmers, G. Schönhense, H. Ebert, C. Felser, and M. Kläui, Nat. Commun. **5**, 3974 (2014).
[29] S. Kokado, M. Tsunoda, K. Harigaya, and A. Sakuma, J. Phys. Soc. Jpn. **81**, 024705 (2012).
[30] B. Kwon, Y. Sakuraba, H. Sukegawa, S. Li, G. Qu, T. Furubayashi, and K. Hono, J. Appl. Phys. **119**, 023902 (2016).
[31] Y. Sakuraba, S. Kokado, Y. Hirayama, T. Furubayashi, H. Sukegawa, S. Li, Y. K. Takahashi, and K. Hono, Appl. Phys. Lett. **104**, 172407 (2014).
[32] F. J. Yang, Y. Sakuraba, S. Kokado, Y. Kota, A. Sakuma, and K. Takanashi, Phys. Rev. B **86**, 020409(R) (2012).
[33] S. Li, Y. K. Takahashi, Y. Sakuraba, N. Tsuji, H. Tajiri, Y. Miura, J. Chen, T. Furubayashi, and K. Hono, Appl. Phys. Lett. **108**, 122404 (2016).
[34] K. Goto, L. S. R. Kumara, Y. Sakuraba, Y. Miura, I. Kurniawan, A. Yasui, H. Tajiri, Y. Fujita, Z. Chen, and K. Hono, Phys. Rev. Mater. **4**, 114406 (2020).
[35] Y. K. Takahashi, A. Srinivasan, B. Varaprasad, A. Rajanikanth, N. Hase, T. M. Nakatani, S. Kasai, T. Furubayashi, and K. Hono, Appl. Phys. Lett. **98**, 152501 (2011).
[36] J. W. Jung, Y. Sakuraba, T. T. Sasaki, Y. Miura, and K. Hono, Appl. Phys. Lett. **108**, 102408 (2016).
[37] S. Takahashi and S. Maekawa, Phys. Rev. B **67**, 052409 (2003).
[38] J. Korringa, Physica **13**, 392 (1947).
[39] W. Kohn and N. Rostoker, Phys. Rev. **94**, 1111 (1954).
[40] M. Däne, M. Lüders, A. Ernst, D. Ködderitzsch, W. M. Temmerman, Z. Szotek, and W. Hergert, J. Phys.: Condens. Matter **21**, 045604 (2009).
[41] J. P. Perdew and Y. Wang, Phys. Rev. B **45**, 13244 (1992).
[42] K. Momma and F. Izumi, J. Appl. Crystallogr. **44**, 1272 (2011).
[43] O. Sakata, Y. Furukawa, S. Goto, T. Mochizuki, T. Uruga, K. Takeshita, H. Ohashi, T. Ohata, T. Matsushita, S. Takahashi, H. Tajiri, T. Ishikawa, M. Nakamura, M. Ito, K. Sumitani, T. Takahashi, T. Shimura, A. Saito, and M. Takahasi, Surf. Rev. Lett. **10**, 543 (2003).
[44] H. Tajiri, H. Yamazaki, H. Ohashi, S. Goto, O. Sakata, and T. Ishikawa, J. Synchrotron Rad. **26**, 750 (2019).
[45] See Supplemental Material at http://link.aps.org/supplemental/10.1103/PhysRevMaterials.6.064411 for details on theoretical calculations of standard CFGG and structural analysis of Co-rich CFGG.
[46] B. S. D. C. S. Varaprasad, A. Srinivasan, Y. K. Takahashi, M. Hayashi, A. Rajanikanth, and K. Hono, Acta Mater. **60**, 6257 (2012).
[47] I. Kurniawan, K. Nawa, K. Masuda, Y. Miura, and K. Hono, Acta Mater. **218**, 117218 (2021).
[48] J. Bass and W. P. Pratt, J. Phys.: Condens. Matter **19**, 183201 (2007).
[49] A. N. Pohorilyi, A. F. Kravetz, E. V. Shipil, A. Y. Vovk, C. S. Kim, and H. R. Khan, J. Magn. Magn. Mater. **186**, 87 (1998).
[50] H. Funaki, S. Okamoto, O. Kitakami, and Y. Shimada, Jpn. J. Appl. Phys. **33**, L1304 (1994).
[51] L. Tong, M. Pan, J. Long, M. Lu, X. Wu, A. Hu, and H. Zhai, J. Magn. Magn. Mater. **226–230**, 1749 (2001).
[52] L. Ding, J. Teng, Q. Zhan, C. Feng, M. H. Li, G. Han, L. J. Wang, G. H. Yu, and S. Y. Wang, Appl. Phys. Lett. **94**, 162506 (2009).